A numerical study on the aeroacoustics of a propeller at low Reynolds number subjected to vortical gusts

QUIET DRONES 2026
Delft, 29th June - 1st July 2026

A numerical study on the aeroacoustics of a propeller at low Reynolds number subjected to vortical gusts

Session: UAS/UAM noise modeling 1

Mario Alì, Department of Mechanical and Aerospace Engineering, Politecnico di Torino, Corso Duca degli Abruzzi, 24, Torino, Italy, mario.ali@polito.it
Andrea Piccolo, Department of Flow Physics and Technology, Aerospace Engineering Faculty, Delft University of Technology, Kluyverweg 1, Delft, 2629 HS, The Netherlands, a.piccolo@tudelft.nl
Riccardo Zamponi, Department of Flow Physics and Technology, Aerospace Engineering Faculty, Delft University of Technology, Kluyverweg 1, Delft, 2629 HS, The Netherlands, r.zamponi@tudelft.nl
Daniele Ragni, Department of Flow Physics and Technology, Aerospace Engineering Faculty, Delft University of Technology, Kluyverweg 1, Delft, 2629 HS, The Netherlands, d.ragni@tudelft.nl
Francesco Avallone, Department of Mechanical and Aerospace Engineering, Politecnico di Torino, Corso Duca degli Abruzzi, 24, Torino, Italy, francesco.avallone@polito.it

Abstract Drones operating in an urban environment are exposed to turbulent flows generated by atmospheric boundary layers, obstacles, and temperature gradients. This work investigates the aeroacoustics of a low-Reynolds-number propeller in forward flight subjected to sinusoidal gusts. Very Large Eddy Simulations based on the Lattice Boltzmann Method are performed with the commercial software PowerFLOW. Gusts are introduced through unsteady inlet boundary conditions, ensuring the divergence-free condition. Results show that gusts generate additional tonal noise at frequencies given by a combination of the gust frequency and multiples of the rotational frequency, as a result of an amplitude/phase modulation mechanism.

Keywords: Low-Reynolds propeller; Gust; Tonal noise; Phase/amplitude modulation

1. Introduction

Urban environments exhibit large-scale anisotropic turbulence generated by atmospheric boundary layers, surrounding obstacles, and thermal gradients (Kaimal & Finnigan, 1994; Monin, 1970; Liu et al., 2017). They are especially significant for small propellers, that operate at low Reynolds numbers, as their aerodynamic performances are particularly sensitive to inflow disturbances (Casalino et al., 2022). Most studies on propeller–turbulence interaction use turbulence grids to generate nearly isotropic inflow conditions (Jamaluddin et al., 2021; Go et al., 2024). In most of the studies in literature, ingested turbulence mainly increases broadband noise at mid frequencies, especially above the 2nd BPF, while the high-frequency content remains mostly unaffected (Alì et al., 2026). Large-scale anisotropic disturbances, instead, have been studied by placing propellers in the wake of bluff bodies (Glegg et al., 2017; Trascinelli et al., 2025; Hanson et al., 2024; Yauwenas et al., 2019), typically characterized by the presence of a dominant shedding frequency. In addition to higher broadband noise levels at lower frequencies, sideband peaks around the first harmonic were also observed. The origin of this feature is still not clear.

The objective of this work is to assess the effects of large-scale disturbances on the aeroacoustics of a propeller operating at low Reynolds numbers. The effect of disturbances is studied by investigating, through a parametric study, the response of a propeller to a single-frequency harmonic gust varying its amplitude, lenght scale and direction (Gill et al., 2013; Zhong et al., 2018; Yu et al., 2025; Danao et al., 2014; Wu, 2019). This approach allows the identification of interaction mechanisms associated with individual spectral components and can therefore be regarded as a building block of the broader propeller–turbulence interaction.

2. METHODOLOGY

High-fidelity simulations are performed using the commercial software PowerFLOW. The numerical approach is based on a Lattice–Boltzmann framework (Chen & Doolen, 1998), which is widely employed for the aeroacoustic analysis of propellers and rotors (Casalino et al., 2022; Romani et al., 2022; Yu et al., 2025).

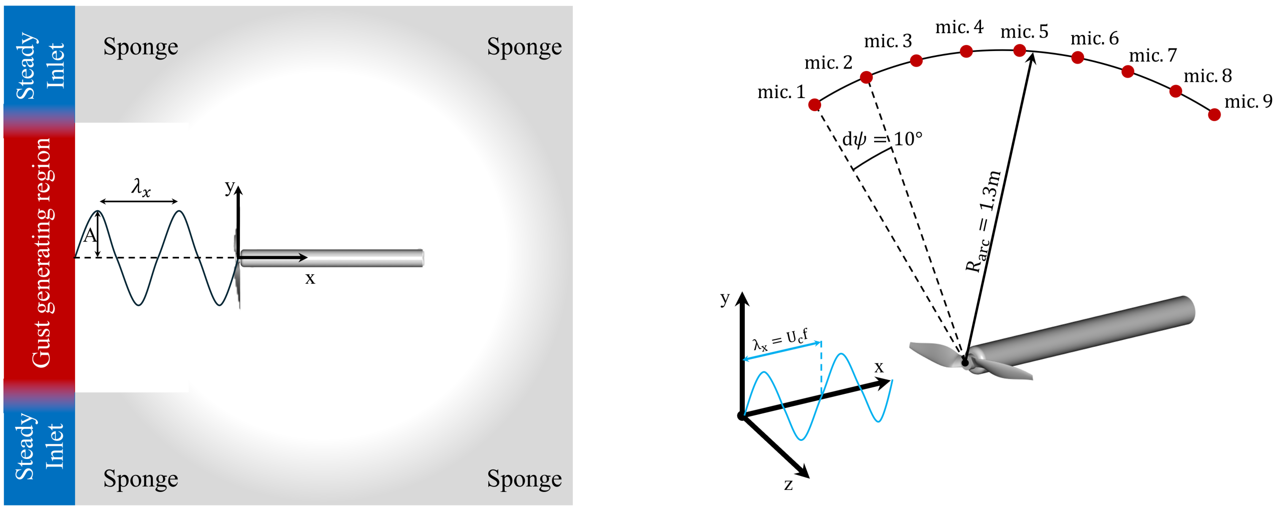

Figure 1: (a) Sketch of the numerical setup and (b) microphones location.

A sketch of the numerical setup is shown in Fig. 1. The streamwise direction is aligned with the x-axis, while u, v, w denote the velocity components along x, y, z. The propeller, characterized in previous studies (Casalino et al., 2021; Grande et al., 2022), is positioned $15\,D$ downstream of the inlet and operates at $\Omega = 6000\,RPM$ with a mean inflow velocity $U_\infty = 10\,ms^{-1}$. The gust is superimposed to the mean inflow through an unsteady inlet boundary condition following Zhong et al. (2018). The gust velocity components are:

$$
\begin{aligned}
&\mathrm{u_{gust}(x,y,t)} = -\mathrm{g(y)h(z)}\frac{\mathrm{Ak_y}}{\sqrt{\mathrm{k_x^2+k_y^2}}}\sin\left(\mathrm{k_x x + k_y y} - \omega_{\mathrm{gust}}\mathrm{t}\right) + \mathrm{g'(y)h(z)}\frac{\mathrm{A}}{\sqrt{\mathrm{k_x^2+k_y^2}}}\cos\left(\mathrm{k_x x + k_y y} - \omega_{\mathrm{gust}}\mathrm{t}\right),\\
&\mathrm{v_{gust}(x,y,t)} = \mathrm{g(y)h(z)}\frac{\mathrm{Ak_x}}{\sqrt{\mathrm{k_x^2+k_y^2}}}\sin\left(\mathrm{k_x x + k_y y} - \omega_{\mathrm{gust}}\mathrm{t}\right),\\
&\mathrm{w_{gust}(x,y,t)} = 0.
\end{aligned}
\tag{1}
$$

Here, A is the gust amplitude, k_x and k_y are the longitudinal and transverse wave numbers, and $\omega_{\text{gust}} = U_\infty k_x$ is the gust angular frequency. The smooth functions $g(y)$ and $h(z)$ localize the gust within a region of the inlet, out of which only the steady inflow velocity is imposed. Eq.1 is such that the velocity divergence-free condition is verified, thus avoiding the formation of spurious acoustic waves. Sponge zones are applied near the domain boundaries to reduce reflections. The computational mesh consists of 15 regions (*VR*s) with a uniform voxel size in each region. In the region with the lowest resolution there are at least 10 voxels per gust wavelength, while in the refined inner regions around the propeller the resolution is such to resolve the relevant flow structures (Casalino et al., 2022).

Far-field acoustics is predicted by applying the solid formulation of the Ffowcs Williams – Hawkings (FW-H) acoustic analogy (Ffowcs Williams & Hawkings, 1969) using the unsteady surface pressure data sampled on the propeller and nacelle surface. The far-field noise is computed at the microphone positions shown in Fig. 1b. Quadrupole sources are neglected due to the low Mach number (Glegg & Devenport, 2017).

Besides the steady inflow case, five gust configurations (Table 1) are considered, varying frequency $\mathrm{f_{gust}}$, initial phase ϕ_0, and direction α of the gust. The gust amplitude is fixed at 10% of $\mathrm{U_\infty}$.

Table 1: Gusts tested in the study

Gust	$\mathrm{k_x}/2\pi$ [cm^{-1}]	$\mathrm{k_y}/2\pi$ [cm^{-1}]	$\mathrm{f_{gust}/f_{rot}}$	ϕ_0 [°]	α [°]
Gust 1	1/10	0	1	0	0
Gust 2	1/15	0	2/3	0	0
Gust 3	1/20	0	1/2	0	0
Gust 4	1/10	0	1	90	0
Gust 5	1/10	1/10	1	0	45

3. Analytical prediction

The vortical gust causes a time-variation of the blade angle of attack through two mechanisms: perturbing the upwash velocity and/or modulating the effective tangential velocity. In the next section, how this affects the unsteady loading is explained.

3.1 Unsteady loading

Considering a single blade element at radius r rotating in the yz-plane, the upwash gust velocity component in the relative frame of reference can be written as:

$$\mathrm{u_{gust}(r,t)} = -\frac{\mathrm{Ak_y}}{\sqrt{\mathrm{k_x^2+k_y^2}}}\mathrm{s(r,t)}, \tag{2}$$

with

$$s(r,t) = \sin\left[k_y r \sin(\omega_{rot} t + \phi_0) - \omega_{gust} t\right]. \tag{3}$$

This shows that blade rotation introduces a phase modulation. This expression can be expanded as:

$$s(r,t) = \sum_{n=-\infty}^{\infty} J_n(k_y r) \sin\left[(n\omega_{rot} - \omega_{gust})t + n\phi_0\right], \tag{4}$$

which shows that the phase modulation produces peaks in the unsteady inflow spectrum seen by the blade at:

$$\omega = n\omega_{rot} - \omega_{gust}, \qquad n \in \mathbb{Z}. \tag{5}$$

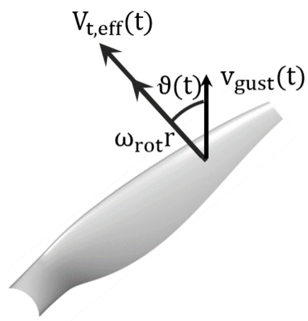

Figure 2: Effective tangential velocity modulation

The effective tangential velocity experienced by the blade element is given by the sum of the tangential velocity $V_t = \omega_{rot} r$ and the projection along the tangential direction of the gust-induced velocity (Fig. 2):

$$V_{t,eff}(t) = \omega_{rot} r + v_{gust}(t) \cos(\theta(t)). \tag{6}$$

The unsteady velocity term in the above equation can be expanded as:

$$\frac{A k_y}{\sqrt{k_x^2 + k_y^2}} \left[\sum_{n=-\infty}^{\infty} J_n(k_y r) \sin\left[(n\omega_{rot} - \omega_{gust})t + n\phi_0\right]\right] \cos(\omega_{rot} t + \phi_0). \tag{7}$$

This shows that the interaction between the gust and the rotational motion modulates the effective tangential velocity both in phase and amplitude. This modulation leads to an unsteady inflow spectrum with peaks at:

$$\omega = (n \pm 1)\omega_{rot} - \omega_{gust}, \qquad n \in \mathbb{Z}. \tag{8}$$

For the limit case $k_y r \to 0$ (spanwise-uniform gust), the interaction reduces to a pure amplitude modulation, yielding discrete frequencies at $\omega_{rot} \pm \omega_{gust}$.

The frequencies in the unsteady inflow spectrum are transferred to the angle of attack and, under linear aerodynamic assumptions, to the unsteady lift response, which inherits the same spectral content through the Theodorsen function (Sears, 1941; Gülçat, 2010).

3.2 Far-field noise

In this section, Lowson' s theory (Lowson, 1965) is adopted to explain how the unsteady loading is acoustically radiated to the far-field at frequencies shifted by multiples of the rotational frequency. By modelling each blade as an equivalent rotating force $\vec{F} = (F_1, F_2, F_3)$, the far-field acoustic pressure is given by:

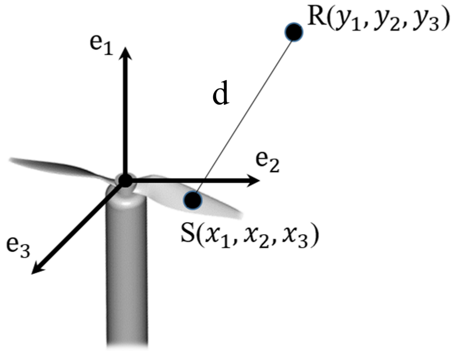

Figure 3: Absolute frame of reference adopted in the description of the analytical framework. $S(x_1,x_2,x_3)$ denotes the source point, while $R(y_1,y_2,y_3)$ is the receiver.

$$p(\vec{\mathbf{x}},t) = \left[\frac{(x_i - y_i)}{4\pi a_0 d^2 (1 - M_r)^2} \left(\frac{\partial F_i}{\partial t} + \frac{F_i}{1 - M_r} \frac{\partial M_r}{\partial t} \right) \right]_{t=\tau} . \tag{9}$$

Here, x_i and y_i denote the i-th coordinates of the source and observer, respectively, M_r is the relative Mach number of the source with respect to the observer, and d is their separation distance (Fig. 3). The expression in Eq.9 must be evaluated at the emission time τ (Lowson, 1965; Glegg & Devenport, 2017). The overall acoustic pressure is given by the sum of two contributions: the unsteady loading term ($\partial F_i/\partial t$) and the loading-in-motion term ($F_i\, \partial M_r/\partial t$). Both of the contributions are multiplied by a term expressing the relative position and distance of the source with respect to the observer:

$$q(t) = \frac{(x_i - y_i)}{4\pi a_0 d^2 (1 - M_r)^2}, \tag{10}$$

which, in the case of rotational motion, can be expressed as a periodic Fourier series. Writing the unsteady blade loading as Fourier series gives:

$$p(\vec{\mathbf{x}},t) \sim \sum_{n=-\infty}^{+\infty} \sum_{\lambda} \hat{q}_n \hat{F}_{i,\lambda}\, e^{j(\omega_\lambda + n\omega_{rot})\tau}, \tag{11}$$

where $\hat{(\cdot)}$ denotes the Fourier coefficient and ω_λ is the λ-th harmonic in the unsteady loading spectrum. This shows that the unsteady loading peaks are shifted by multiples of the rotational frequency when acoustically radiated to the far-field. The acoustic spectrum therefore contains tonal noise at frequencies given by:

$$\omega = \omega_\lambda + n\omega_{rot}, \qquad n \in \mathbb{Z}. \tag{12}$$

The amplitude of the resulting acoustic tone depends on the interference between the contributions of the two blades, which may produce constructive or destructive interference depending on their relative phase.

4. Results and Discussion

4.1 Unsteady loading

4.1.1 Effect of frequency

Figure 4 shows the blade thrust history varying the gust frequency. In all cases, the gust induces periodic loading fluctuations due to variations in the effective tangential velocity. The fluctuations on the two blades are always in phase opposition, since an increase in tangential velocity on one blade corresponds to a decrease on the other, leading to opposite variations in angle of attack and sectional loading. Consequently, no effect is visible when looking at the integral thrust and are not visible in the overall rotor loading. For this reason, the unsteady loading spectrum on a single blade is analysed in the next.

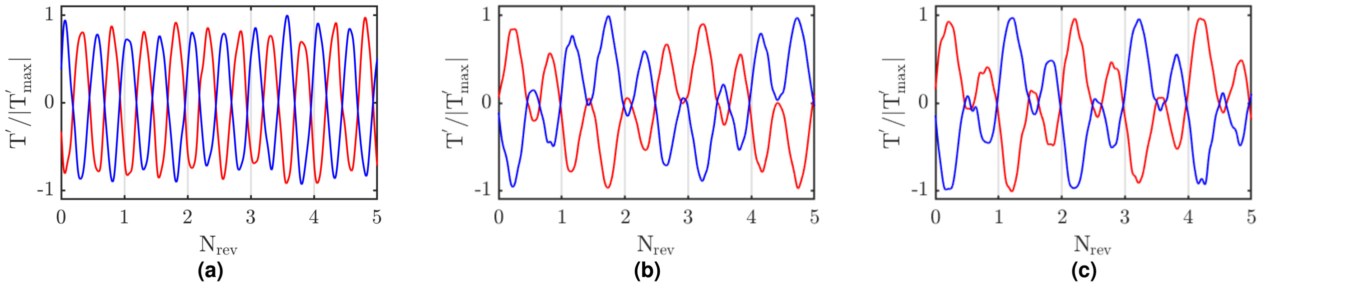

Figure 4: Time-history of the unsteady thrust at (a) $f_{gust}/f_{rot} = 1$, (b) $3/2$ and (c) $1/2$. The blue and red lines refer to the two blades.

Figure 5 shows the spectra of each blade loading for the analyzed gust frequencies. Distinct tonal components appear at frequencies $f_{rot} \pm f_{gust}$. In Figure 5a, only the peak at $f_{rot} + f_{gust}$ is observed, since $f_{rot} = f_{gust}$ in this case. Furthermore, no peak is observed at the gust frequency itself. The emergence of peaks at frequencies mirrored with respect to the rotational frequency confirms that the amplitude modulation of the unsteady loading is related to the amplitude modulation in the effective tangential velocity as described in Section 3.1.

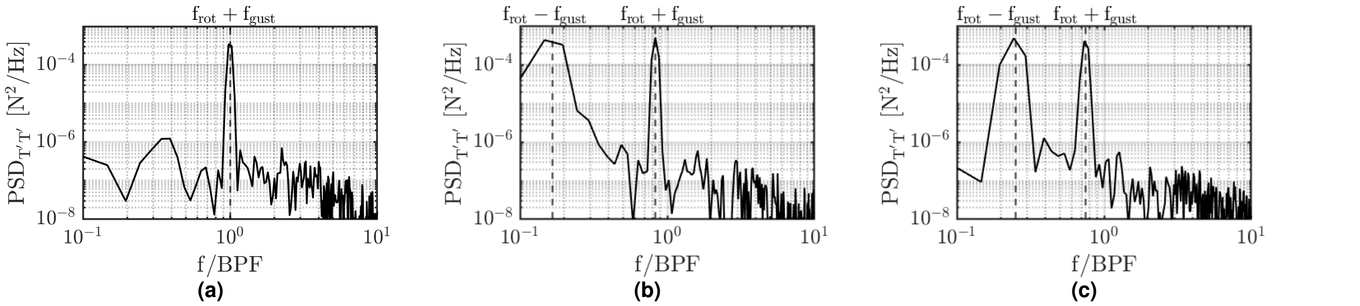

Figure 5: Unsteady thrust spectra for (a) $f_{gust}/f_{rot} = 1$, (b) $3/2$ and (c) $1/2$.

4.1.2 Effect of initial phase

Figure 6 compares the time-history of the blade loading over one revolution for two initial phases: $\phi_0 = 0°$ and $\phi_0 = 90°$. In both cases, the gust frequency is $f_{gust}/f_{rot} = 1$. The two time-histories exhibit a phase shift of about $45°$, which is also reflected in their time derivatives. Referring to Fig.6b, when $\phi_0 = 0°$, the blade experiences the maximum velocity perturbation when it is radially aligned with the gust itself. In this configuration, the gust acts mainly along to the radial direction, therefore with a negligible effect on the angle-of-attack. When the blade is nearly perpendicular to the gust, the perturbation is the smallest. As a result, the maximum variation of the angle of attack will occur in between these two conditions. Instead, when $\phi_0 = 90°$, the blade experiences the maximum velocity perturbation along the chord. This coincides with the maximum variation in the angle of attack with respect to the steady condition. This explains the phase shift observed in Fig.6a. However, it can be observed that the maximum loading perturbation with respect to the steady condition occurs slightly before $\phi = 180°$ and $225°$, for $\phi_0 = 90°$ and $0°$, respectively. This is likely due to the flow acceleration induced by the propeller.

Since unsteady loading is a primary noise source, this phase variation is expected to influence the resulting noise directivity.

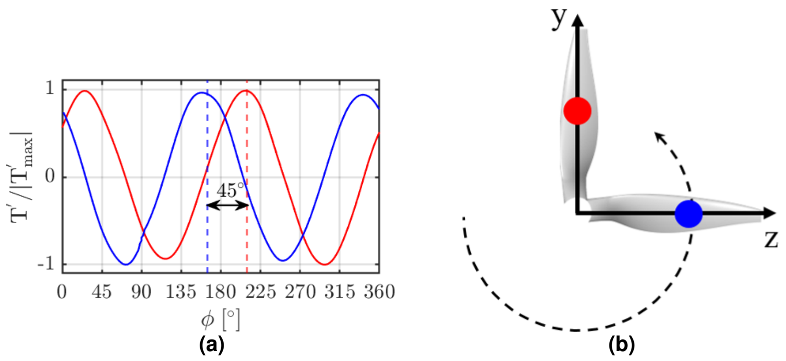

Figure 6: Effect of the initial phase on the time history of (a) unsteady thrust over one revolution and (b) blade positions at the maximum gust induced velocity perturbation for the two initial phases. The blue color refers to $\phi_0 = 90°$, the red to $\phi_0 = 0°$

4.1.3 Effect of gust orientation

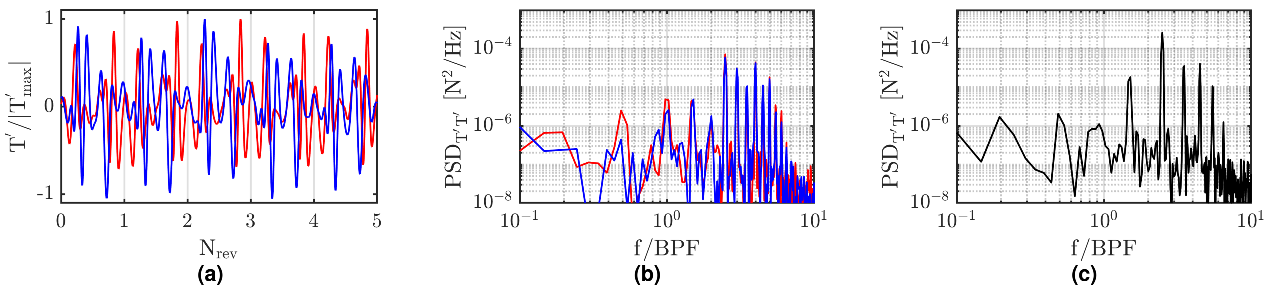

Figure 7: Unsteady thrust with gust at $\alpha = 45°$: (a) time history and (b,c) spectra for the single blades and the overall rotor, respectively. The blue and red lines refer to the two blades.

Figure 7 compares the unsteady loading spectra for gust directions $\alpha = 0°$ and $\alpha = 45°$. When the gust is inclined ($\alpha = 45°$), both in-plane and out-of-plane velocity components vary along the rotor diameter, producing a more complex angle-of-attack distribution. This results in an unsteady loading spectrum characterised by higher harmonics. The unsteady loading spectrum is reported both for the single blades (Fig.7a) and the entire rotor (Fig.7b). For both spectra, the loading response at f_{gust} remains weak, while higher harmonics are more pronounced, as a result of the more complex angle-of-attack distribution. More in detail, the individual blade loading (Fig. 7b) exhibits both BPF harmonics and interharmonics, while the total loading (Fig. 7c) contains only interharmonics, thus indicating cancellation of the BPF harmonics between blades due to phase opposition. As in the previous cases, the peaks are observed at frequencies that are combinations of the gust frequency and multiples of the rotational frequency. In particular, BPF interharmonics satisfy $nf_{rot} \pm f_{gust}$ for even n, whereas harmonics correspond to odd n.

4.2 Far-field noise

For completeness, the far-field noise spectra are reported up to the 100^{th} BPF harmonic. However, since no effect was observed on the 1^{st} and 2^{nd},BPF harmonics or on the high-frequency broadband floor, the discussion focuses on the additional tonal noise introduced by the interaction with the gust. The acoustic spectra presented in the following refer to mic. 1. The reference pressure is $p_{ref} = 2 \times 10^{-5}$ Pa.

4.2.1 Effect of gust frequency

Figure 8 compares the acoustic spectra for gust cases 1–3 in Table 1 against the clean configuration. Additional tones appear at f_{gust} and $BPF \pm f_{gust}$. Since the gust does not gen-

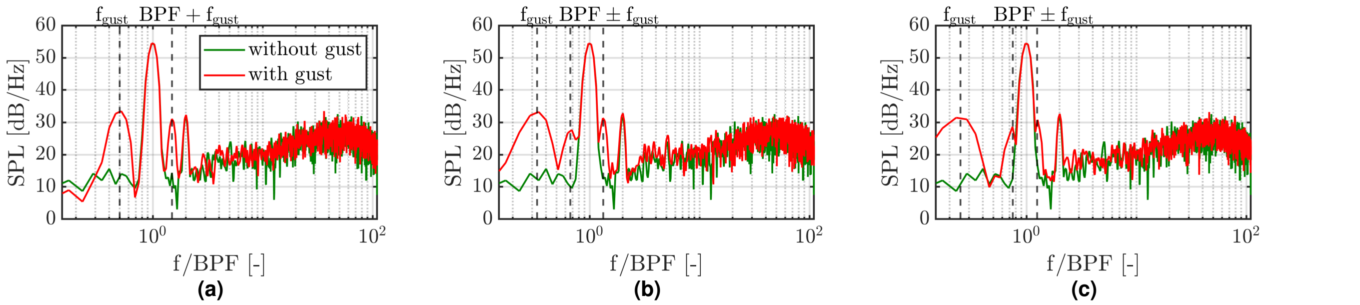

Figure 8: Acoustic spectra for (a) $f_{gust}/f_{rot} = 1$, (b) $3/2$ and (c) $1/2$.

erate noise, the propeller is the only acoustic source at f_{gust}. Similar features were observed in propeller–wake interaction studies (Trascinelli et al., 2025; Yauwenas et al., 2019), suggesting a common noise-generation mechanism Considering the unsteady loading spectra (Fig.5) and the analytical approach in Section 3.2, we can conclude that the unsteady loading fluctuations, generated by the modulation of the effective tangential velocity, have been frequency-shifted by multiples of the rotational frequency when acoustically radiated, as a consequence of the rotational motion of the blades.

4.2.2 Effect of gust phase

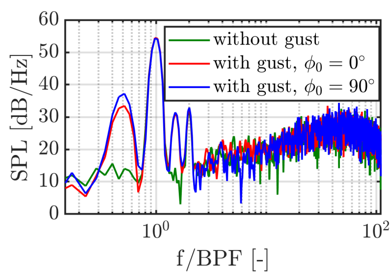

Figure 9: Effect of initial phase on acoustic spectrum at mic.1.

Figure 9 shows the effect of ϕ_0 on the acoustic spectrum when $f_{gust}/f_{rot} = 1$. In agreement with the unsteady loading results in Fig. 6a, both configurations exhibit the same additional tonal components. However, when $\phi_0 = 0°$, the amplitude of the peak at $BPF - f_{gust}$ is reduced, suggesting a change in directivity, whereas the tone at $BPF + f_{gust}$ remains unaffected.

Figure 10 confirms this and illustrates the effect of ϕ_0 on the directivity of the tones at $BPF \pm f_{gust}$. The influence is stronger at $BPF - f_{gust}$, where $\phi_0 = 0°$ leads to lower SPL and a rotation of the directivity pattern compared to $\phi_0 = 90°$. For $\phi_0 = 90°$, the radiation is the strongest along the velocity fluctuation direction, whereas for $\phi_0 = 0°$ it shifts opposite to the propeller rotation. In contrast, the $BPF + f_{gust}$ tone shows similar levels and directivity for both phases, with maximum radiation downstream of the propeller. Overall, the initial phase mainly affects the directivity of the lower-frequency tonal noise, explaining the SPL difference at $BPF - f_{gust}$ observed in Fig. 9.

4.2.3 Effect of gust direction

Figure 11a compares the acoustic spectra at mic. 1 for the clean inflow and the cases 1 and 5 in Table 1. When the gust is inclined ($\alpha = 45°$), the spectrum becomes more complex, with tonal peaks extending up to the 10^{th} BPF harmonic. Apart from the 1^{st} and 2^{nd} BPF harmonics, only interharmonic peaks are observed. It is interesting to observe that, similarly to the previous cases, the acoustic frequencies observed coincide with the peaks in phase opposition in the unsteady loading spectrum, shifted by the rotational frequency. Interestingly, no peak appears at f_{gust}, despite its presence in the upwash velocity spectrum. Fig.11b shows

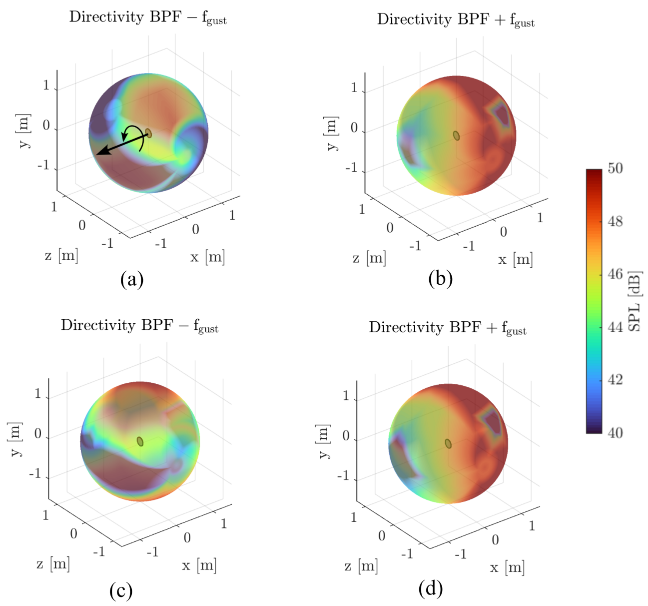

Figure 10: Directivity of unsteady loading noise for $\phi_0 = 0°$ and $90°$.

the contributions of the two blades to the overall acoustic spectrum. A pronounced peak can be observed in the single-blade acoustic spectra, indicating that the absence of a peak at f_{gust} in the total spectrum results from destructive interference between the acoustic waves radiated by the two blades at f_{gust}.

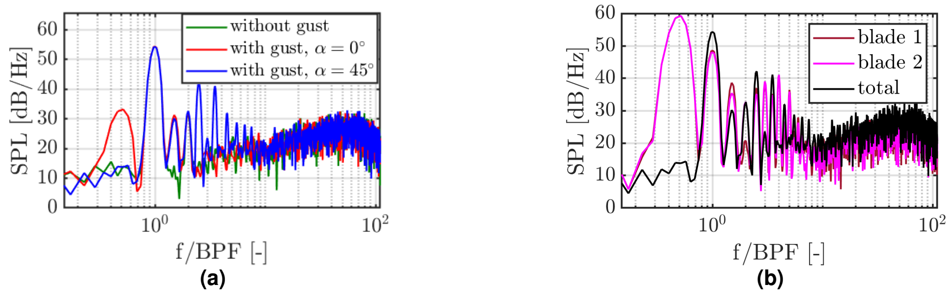

Figure 11: (a) Effect of gust direction on acoustic spectrum at mic.1 and (b) contribution from each blade.

5. Conclusions

High-fidelity numerical simulations were used to study the aeroacoustics of a low-Reynolds-number propeller in advancing flight subjected to harmonic gusts. Additional tonal components were observed to arise in the far-field noise spectra because of the unsteady loading due to interaction of the propeller with the gust. The additional tones are located at frequencies given by a combination of the gust frequency and multiples of the rotational frequency. More in detail, spanwise-uniform gusts produce amplitude modulation of blade loading, generating components at $f_{rot} \pm f_{gust}$, which radiate at $BPF \pm f_{gust}$ and at f_{gust}. The gust initial phase influences loading phase and low-frequency directivity. For gusts inclined with respect to the propeller axis of rotation, multiple loading peaks appear, extending the impact on the far-field noise up to the 10^{th} BPF harmonic. In general, these features are the outcome of a two-step modulation process involving blade rotation and acoustic radiation, with additional inter-blade interference. Overall, the results contribute to a better understanding of the interaction between periodic large-scale gusts and rotating blades, supporting improved prediction models for unsteady loading noise.

Future work will include additional high-fidelity simulations at higher advance ratios to assess the influence of steady loading conditions, comparisons with low-fidelity tools to evaluate their reliability under these inflow conditions, and an extension of the range of investigated gust cases.

Acknowledgments

Authors would like to thank Institution Fondazione Compagnia di San Paolo for financial support.

References

Alì, M., Piccolo, A., Zamponi, R., Ragni, D., & Avallone, F. (2026). On the aeroacoustics of a propeller at low reynolds number subjected to a grid-induced turbulent inflow. *Aerospace Science and Technology*, 112114.

Casalino, D., Grande, E., Romani, G., Ragni, D., & Avallone, F. (2021). Definition of a benchmark for low Reynolds number propeller aeroacoustics. *Aerospace Science and Technology*, *113*, 106707.

Casalino, D., Romani, G., Zhang, R., & Chen, H. (2022). Lattice-boltzmann calculations of rotor aeroacoustics in transitional boundary layer regime. *Aerospace Science and Technology*, *130*, 107953.

Chen, S., & Doolen, G. D. (1998). Lattice boltzmann method for fluid flows. *Annual review of fluid mechanics*, *30*(1), 329–364.

Danao, L. A., Edwards, J., Eboibi, O., & Howell, R. (2014). A numerical investigation into the influence of unsteady wind on the performance and aerodynamics of a vertical axis wind turbine. *Applied Energy*, *116*, 111–124.

Ffowcs Williams, J. E., & Hawkings, D. L. (1969). Sound generation by turbulence and surfaces in arbitrary motion. *Philosophical Transactions of the Royal Society of London. Series A, Mathematical and Physical Sciences*, *264*(1151), 321–342. doi: 10.1098/rsta.1969.0031

Gill, J. R., Zhang, X., & Joseph, P. (2013). Effects of real airfoil geometry on leading edge gust interaction noise. In *19th aiaa/ceas aeroacoustics conference* (p. 2203).

Glegg, S., & Devenport, W. (2017). *Aeroacoustics of low mach number flows: fundamentals, analysis, and measurement*. Academic Press.

Glegg, S., Grant, J., Devenport, W. J., & Alexander, W. N. (2017). Sound radiation from a rotor operating in the wake of a cylinder. In *55th aiaa aerospace sciences meeting* (p. 1172).

Go, S. T., Kingan, M. J., Bowen, L., & Azarpeyvand, M. (2024). Noise of a shrouded propeller due to ingestion of grid-generated turbulence. *Journal of Sound and Vibration*, *571*, 118044.

Grande, E., Romani, G., Ragni, D., Avallone, F., & Casalino, D. (2022). Aeroacoustic investigation of a propeller operating at low Reynolds numbers. *AIAA Journal*, *60*(2), 860–871.

Gülçat, Ü. (2010). *Fundamentals of modern unsteady aerodynamics* (Vol. 2010). Springer.

Hanson, L. P., Zang, B., & Azarpeyvand, M. (2024). Experimental characterisation of cylinder-induced turbulence ingestion in propellers operating in edgewise flight. In *30th aiaa/ceas aeroacoustics conference (2024)* (p. 3100).

Jamaluddin, N. S., Celik, A., Baskaran, K., Rezgui, D., & Azarpeyvand, M. (2021). Aeroacoustic performance of propellers in turbulent flow. In *Aiaa aviation 2021 forum* (p. 2188).

Kaimal, J. C., & Finnigan, J. J. (1994). *Atmospheric boundary layer flows: their structure and measurement*. Oxford university press.

Liu, J., Niu, J., Mak, C. M., & Xia, Q. (2017). Detached eddy simulation of pedestrian-level wind and gust around an elevated building. *Building and Environment*, *125*, 168–179.

Lowson, M. (1965). The sound field for singularities in motion. *Proceedings of the Royal Society of London. Series A. Mathematical and Physical Sciences*, *286*(1407), 559–572.

Monin, A. (1970). The atmospheric boundary layer. *Annual Review of Fluid Mechanics*, *2*(1), 225–250.

Romani, G., Grande, E., Avallone, F., Ragni, D., & Casalino, D. (2022). Computational study of flow incidence effects on the aeroacoustics of low blade-tip mach number propellers. *Aerospace Science and Technology*, *120*, 107275.

Sears, W. R. (1941). Some aspects of non-stationary airfoil theory and its practical application. *Journal of the Aeronautical Sciences*, *8*(3), 104–108.

Trascinelli, L., Romani, G., Hanson, L., Casalino, D., Zang, B., Zhou, B. Y., & Azarpeyvand, M. (2025, 07). Numerical simulations of large-scale turbulence ingestion by a forward flight propeller. *The Journal of the Acoustical Society of America*, *158*(1), 826-837. doi: 10.1121/10.0037219

Wu, Z. (2019). Rotor power performance and flow physics in lateral sinusoidal gusts. *Energy*, *176*, 917–928.

Yauwenas, Y., Fischer, J. R., Moreau, D., & Doolan, C. J. (2019). The effect of inflow disturbance on drone propeller noise. In *25th aiaa/ceas aeroacoustics conference* (p. 2663).

Yu, H., Shao, M., & Jiang, H. (2025). Numerical study on the time-harmonic gust response of a vertical axis wind turbine. *Physics of Fluids*, *37*(1).

Zhong, S., Zhang, X., Gill, J., Fattah, R., & Sun, Y. (2018). A numerical investigation of the airfoil-gust interaction noise in transonic flows: Acoustic processes. *Journal of Sound and Vibration*, *425*, 239–256.